Crack growth in non-homogeneous transformable ceramics. Part II

Stam, Geert; Giessen, Erik van der

Published in:
International Journal of Fracture

DOI:
10.1007/BF00019381

International Journal of Fracture **79:** 273–293, 1996.

Crack growth in non-homogeneous transformable ceramics. Part II: Crack deflection

GEERT STAM* and ERIK VAN DER GIESSEN
Delft University of Technology, Laboratory for Engineering Mechanics, Delft, The Netherlands

Received 10 May 1995; accepted in revised form 8 March 1996

Abstract. Crack growth in transformation toughened ceramics is studied using a micromechanics based continuum model which accounts for both dilatant and shear transformation strain components. In the computations, the transformable phase is taken to be distributed non-homogeneously in order to model Zirconia Toughened Aluminas that have not been optimally mixed, or Duplex Ceramics in which large zirconia inclusion are dispersed in an untransformable matrix. The small scale transformation problem is solved using a finite element approach. The influence of the transformation strains around the propagating crack on the stress intensity at the crack tip is computed using the transformation domain integral. The crack is modelled as a missing row of mesh elements and crack growth is simulated by nullifying the stiffness of a crack tip element. In contrast to Part I of this paper [1], this part is concerned with cases where the transformable phase is not distributed symmetrically with respect to the x_1-axis, which causes the crack to deflect from its original crack path due to a local shear stress intensity factor at the crack tip. A computational method is developed which is capable of simulating this, assuming that the deflections from the original crack path are small. A parametric study is carried out of the effect of crack deflection and crack meandering on the overall crack growth resistance.

1. Introduction

In general, a crack can be deflected from its original crack path due to non-symmetric loading with respect to the crack plane [2, 3] and/or due to the material microstructure [4]. It is well-known [4–8] that crack deflection may have a large influence on the toughness during crack growth. In this two-part paper we study crack growth in transformable ceramics in which the transformable phase (zirconia) is not distributed homogeneously throughout the material. Part I deals with distributions which are presumed to be symmetric with respect to the x_1-axis that is parallel to the initial crack path [1]. Hence, crack propagation takes place along the x_1-axis. Here, in Part II, we consider distributions which are *not* symmetric with respect to the x_1-axis. We shall do so by taking the crack coordinate system (x_1, x_2) to be parallel to the (X_1, X_2)-system of the distribution function $f_D^m(X_1, X_2)$ (2) in [1], but with an offset y_c perpendicular to the initial crack tip such that (see Figure 2 in [1]),

$$X_1 = x_1, \qquad X_2 = x_2 + y_c. \tag{1}$$

As the transformation strain distribution around the propagating crack tip will not be symmetric with respect to the crack plane, crack deflection should be expected under remote mode I loading conditions. The purpose of this study is to get some indication of how crack deflection may affect the overall crack growth resistance, as the crack may now find a path which is energetically more favorable. As in Part I, we shall concentrate on model cases that are considered to be representative for Zirconia Toughened Alumina (ZTA), where the spatial variation in the

* Currently at Rutgers University, College of Engineering, Department of Ceramics, Piscataway, NJ, U.S.A.

fraction of transformable phase varies smoothly according to the distribution function f_D^m, or cases representing Duplex Ceramics where all transformable phase is clustered.

The problem considered here belongs to the large class of crack growth problems, where the crack path is not straight and not known in advance. Numerous proposals for numerical models and simulation techniques have appeared in the literature for these type of problems. Within the framework of continuum finite element models, one finds various nodal release techniques with or without remeshing techniques around the propagating crack tip(s) (e.g. Ingraffea and Saouma [9], and Wang et al. [10] for concrete), element vanish methods (e.g. Tvergaard [11] for elastoplastic damaged solids, Ortiz and Giannakopoulos [12] for monolithic ceramics), and cohesive zone models (e.g. Xu and Needleman [13] for dynamic crack growth in glass). Most of these methods, however, rely on the constitutive behavior of the material under consideration. For the problem at hand, we found that none of the referenced approaches were directly applicable. Therefore, we developed a special purpose approach, which is to a certain extent similar to element vanish techniques, but with a distinct criterion for crack growth.

Compared to Part I, the presence of mixed mode components at the crack tip and of crack deflection requires a new formulation of the crack growth criterion on the basis of both mode I (tensile mode) and mode II (sliding mode), as well as an expression for the direction in which the crack proceeds (see [8]). The approach will be briefly summarized in Section 2. Moreover, a reformulation of the domain integral discussed in [1] is necessary to be able to determine the effect of a single transformed particle on the mode I as well as mode II stress intensity components (Section 3). The current discretization of the boundary value problem, as well as the numerical implementation of the new crack propagation criterion will be discussed in detail (Section 4).

With this novel, dedicated crack growth method, we numerically investigate the crack deflection behavior during crack growth due to transformation strains which develop around the crack. In particular, we study the effect of the position of the crack relative to the regions of high or low fraction of transformable phase as well as the characteristic length of the distribution on the crack growth behavior. Also the effect of other material parameters is considered, such as the strength of the transformation, the amount of twinning, or the possibility of reverse phase transformations.

The constitutive model as well as the finite element formulation of the governing equations have been presented in [1] and will not be repeated. Here, we limit ourselves to reporting the differences in the methodology in order to account for crack deflection.

2. Summary of mixed mode crack analysis

2.1. Crack growth criterion

Throughout the paper we assume that plane strain deformation conditions hold, and the analysis is quasi-static. Often, crack growth is taken to be governed by the energy release rate criterion. The total energy release rate in mixed mode situations $\mathcal{G}$ can be related to the stress intensity factors by the general expression [2]

$$\mathcal{G} = \frac{1-\nu^2}{E}(K_{\mathrm{I}}^2 + K_{\mathrm{II}}^2). \tag{2}$$

Introducing a stress intensity factor K_{tot} through

$$K_{\text{tot}} = \sqrt{K_{\text{I}}^2 + K_{\text{II}}^2}, \tag{3}$$

so that

$$\mathcal{G} = \frac{1-\nu^2}{E} K_{\text{tot}}^2. \tag{4}$$

An alternative criterion is that crack growth occurs when K_{tot} reaches the critical stress intensity of the material K^{C}. The practical validity of this fracture criterion, however, is well-known to be questionable as it implies that $K_{\text{I}}^{\text{C}} = K_{\text{II}}^{\text{C}}$, and that the locus for mixed mode cracking is a circle with radius K_{I}^{C} (cf. e.g. [2]). In practice, $K_{\text{I}}^{\text{C}} \neq K_{\text{II}}^{\text{C}}$; nevertheless we shall use (3) here as our crack growth criterion, since we expect the K_{II} component to be relatively small.

2.2. The direction of crack extension

The two most popular criteria for mixed mode loading that allow crack growth under an angle are (see [14]): (i) the maximum principal stress criterion, which postulates that crack growth occurs in a direction perpendicular to the maximum principal stress, and (ii) the strain energy density criterion, which states that crack growth takes place in the direction of minimum strain energy density. As the difference in predicted angle between the two criteria is rather small, we make an admittedly arbitrary choice and use the maximum principal stress criterion.

It is therefore convenient to express the stresses around the crack tip in polar coordinates. Let us consider the generic situation of an elastic crack tip stress field $\Sigma_{ij}(r,\beta)$ under mixed mode conditions characterized by stress intensity factors K_{I} and K_{II}. Here, r and β are the polar coordinates with respect to the global axes $x_1 - x_2$ as indicated in Figure 3 of [1]. For mode I and mode II loading, respectively, the polar stress components $\Sigma_{rr}, \Sigma_{\beta\beta}$ and $\Sigma_{r\beta}$ are given by [14]

$$\text{Mode I}: \begin{bmatrix} \Sigma_{rr} \\ \Sigma_{\beta\beta} \\ \Sigma_{r\beta} \end{bmatrix} = \frac{K_{\text{I}}}{\sqrt{2\pi r}} \begin{bmatrix} (1+\sin^2\beta/2)\cos\beta/2 \\ (1-\sin^2\beta/2)\cos\beta/2 \\ \cos^2\beta/2 \sin\beta/2 \end{bmatrix};$$

$$\text{Mode II}: \begin{bmatrix} \Sigma_{rr} \\ \Sigma_{\beta\beta} \\ \Sigma_{r\beta} \end{bmatrix} = \frac{K_{\text{II}}}{\sqrt{2\pi r}} \frac{1}{4} \begin{bmatrix} -5\sin\beta/2 + 3\sin 3\beta/2 \\ -3\sin\beta/2 - 3\sin 3\beta/2 \\ \cos\beta/2 + 3\cos 3\beta/2 \end{bmatrix}.$$

The stress fields for combined mode I and II loading are obtained by superposition. The result for $\Sigma_{\beta\beta}(r,\beta)$ and $\Sigma_{r\beta}(r,\beta)$ can be summarized as

$$\begin{aligned} \Sigma_{\beta\beta} &= \frac{1}{\sqrt{2\pi r}}[a_{11}(\beta)K_{\text{I}} + a_{12}(\beta)K_{\text{II}}], \\ \Sigma_{r\beta} &= \frac{1}{\sqrt{2\pi r}}[a_{21}(\beta)K_{\text{I}} + a_{22}(\beta)K_{\text{II}}], \end{aligned} \tag{5}$$

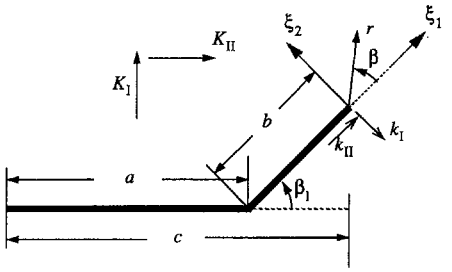

Figure 1. Schematic showing a kinked crack geometry, and definitions of some important variables for the crack analysis.

where

$$a_{11}(\beta) = \tfrac{1}{4}[3\cos\tfrac{1}{2}\beta + \cos\tfrac{3}{2}\beta], \qquad a_{12}(\beta) = -\tfrac{3}{4}[\sin\tfrac{1}{2}\beta + \sin\tfrac{3}{2}\beta],$$
$$a_{21}(\beta) = \tfrac{1}{4}[\sin\tfrac{1}{2}\beta + \sin\tfrac{3}{2}\beta], \qquad a_{22}(\beta) = \tfrac{1}{4}[\cos\tfrac{1}{2}\beta + 3\cos\tfrac{3}{2}\beta]. \tag{6}$$

Now, the angle β_m under which the crack will grow, i.e. the direction perpendicular to the maximum principal stress, is found by equating the shear stress $\Sigma_{r\beta}$ from (5) to zero. We find

$$K_I \sin\beta_m + K_{II}(3\cos\beta_m - 1) = 0, \tag{7}$$

from which it finally follows that β_m is given by one of the two solutions

$$(\tan\tfrac{1}{2}\beta_m)_{1,2} = \frac{1}{4}\frac{K_I}{K_{II}} \pm \sqrt{\left(\frac{K_I}{K_{II}}\right)^2 + 8}, \tag{8}$$

as determined by the maximum (positive) value of $\Sigma_{\beta\beta}(r, (\beta_m)_{1,2})$.

2.3. Analysis of a kinked crack

For linear elastic material behavior, a review of the analysis of kinked cracks has recently been given by Suresh and Shih [15]. The problem under consideration is that of an idealized crack containing a kink of length b inclined at an angle β_1 from the main crack plane, and is shown in Figure 1. The central notion is the relationship between the nominal stress intensity factors K_I and K_{II} (based on the projected crack length c) and the crack tip intensity factors k_I and k_{II} corresponding to a local coordinate system (ξ_1, ξ_2) coinciding with the kinked crack (see Figure 1). In a first approximation, the stress intensity factors at the tip of the kinked crack can be calculated from the stresses that exist in the line of the propagating crack [15]. When K_I and K_{II} denote the stress intensity factors of the main crack in the absence of the kink, then the local stress intensity factors k_I and k_{II}, for the infinitesimal kink ($b/a \to 0$) can be expressed in the form

$$k_I = \lim_{r\to 0+} \sqrt{(2\pi r)}\Sigma_{\beta\beta}(r, \beta_1),$$
$$k_{II} = \lim_{r\to 0+} \sqrt{(2\pi r)}\Sigma_{r\beta}(r, \beta_1), \tag{9}$$

and with (5) we find

$$k_I = a_{11}(\beta_1)K_I + a_{12}(\beta_1)K_I,$$
$$k_{II} = a_{21}(\beta_1)K_I + a_{22}(\beta_1)K_{II}. \tag{10}$$

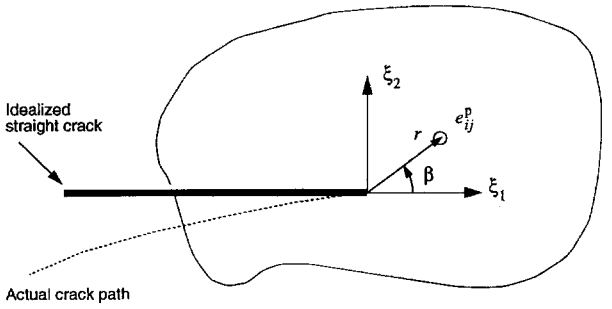

Figure 2. Geometry used for the transformation domain integral.

In our small scale analysis here we implicitly assume that the length of the initial crack c is large compared to the permitted growth of the crack, so that in this situation the kink can be considered infinitesimal. Thus, if an initially straight crack is loaded by far field stress intensities K_α^{APP}, and the crack is kinked, then the corresponding local stress intensity factors k_α^{APP} are calculated using (10) and (6).

As discussed in Part I, the actual local stress intensity factor at the crack tip differs from the applied stress intensity due to the transforming material around the propagating crack. The change of the local stress intensities will be denoted by $\Delta k_\alpha^{\text{TIP}}$, and this will be discussed in detail in the next section. Thus, the stress intensities at the crack tip in the local coordinate system are given by

$$k_\alpha^{\text{TIP}} = k_\alpha^{\text{APP}} + \Delta k_\alpha^{\text{TIP}}. \tag{11}$$

In terms of these local stress intensities, the criterion for crack growth discussed in Section 2.1 becomes

$$K_{\text{tot}} = K_C, \tag{12}$$

where

$$K_{\text{tot}} \sqrt{(k_{\text{I}}^{\text{TIP}})^2 + (k_{\text{II}}^{\text{TIP}})^2}. \tag{13}$$

The direction in which the crack will propagate, relative to the *local* (ξ_1, ξ_2) coordinate system, is determined by

$$(\tan \tfrac{1}{2}\beta_m)_{1,2} = \frac{1}{4}\frac{k_{\text{I}}^{\text{TIP}}}{k_{\text{II}}^{\text{TIP}}} \pm \sqrt{\left(\frac{k_{\text{I}}^{\text{TIP}}}{k_{\text{II}}^{\text{TIP}}}\right)^2 + 8}, \tag{14}$$

according to (8), again taking the angle belonging to the largest principal stress. In the *global* (x_1, x_2) coordinate system, the crack propagation direction is

$$\beta_g = \beta_1 + \beta_m. \tag{15}$$

3. The transformation domain integral

As mentioned in the previous section, the change in stress intensities $\Delta k_\alpha^{\text{TIP}}$ due to the transformation strains needs to be determined relative to the local coordinate system (ξ_1, ξ_2)

at the tip of the kinked crack. We shall do so by an extension of the transformation domain integral technique used in Part I [1]. Before discussing this, it is pointed out that the method is formally limited to straight cracks. For the present problem, curved or even meandering cracks are expected. However, as will be demonstrated in Section 5, the deviations from a straight crack remain small compared to the size of the transformation zone. Therefore, for the evaluation of $\Delta k_\alpha^{\mathrm{TIP}}$, we replace the actual crack by a representative straight crack with corresponding axes (ξ_1, ξ_2). The procedure of establishing such a representative crack will be discussed in Section 4. The geometry used for the application of the domain integral, to be discussed presently, is illustrated in Figure 2.

The transformation domain integral technique used in [1] is based on results obtained by Hutchinson [16] for two transforming spots which are placed *symmetrically* on either side of the straight crack in an infinite plate. This makes the method not applicable to *non-symmetric* transformation zones, as considered here. Gao [17], however, derived a solution for the interaction between the crack tip and a single source of internal strain. The analysis is based on work by Rice [18], using three-dimensional 'weight functions' theory, and on Bueckner's [19] solution for the complete set of weight functions for a half infinite crack. We shall restrict ourselves here to summarizing the results for two-dimensional weight functions and transformation strains.

According to Gao [17], the influence of the transformation strains inside an infinitesimal spot with area $\mathrm{d}A$, located at (ξ_1, ξ_2), on the local stress intensity at the crack tip is given by

$$dk_\alpha^{\mathrm{TIP}} = 2G\overline{U}_{ij}^{\alpha}(\xi_1, \xi_2) e_{ij}^{p}(\xi_1, \xi_2)\, \mathrm{d}A, \tag{16}$$

where G is the elastic shear modulus. The transformation strain components e_{ij}^p in (16) are the transformation strains E_{kl}^p according to the constitutive equations outlined in Part I (see e.g. (29) [1]), but transformed to the local coordinate system which is oriented at an angle β_1 (see Figure 1), i.e.

$$e_{ij}^{p} = R_{ik} E_{kl}^{p} R_{jl}, \qquad R_{ij} = \begin{bmatrix} \cos\beta_1 & \sin\beta_1 & 0 \\ -\sin\beta_1 & \cos\beta_1 & 0 \\ 0 & 0 & 1 \end{bmatrix}. \tag{17}$$

The components $\overline{U}_{ij}^{\alpha}$ in (16) are defined by, in terms of polar coordinates measured from the origin of the local coordinate system,
Mode I:

$$\begin{aligned} \overline{U}_{11}^{\mathrm{I}} &= \frac{C}{8}\frac{1}{r^{3/2}}[\cos\tfrac{3}{2}\beta + 3\cos\tfrac{7}{2}\beta], \qquad \overline{U}_{33}^{\mathrm{I}} = \nu C \frac{1}{r^{3/2}}\cos\tfrac{3}{2}\beta, \\ \overline{U}_{22}^{\mathrm{I}} &= \frac{C}{8}\frac{1}{r^{3/2}}[7\cos\tfrac{3}{2}\beta - 3\cos\tfrac{7}{2}\beta], \qquad \overline{U}_{12}^{\mathrm{I}} = \frac{3C}{8}\frac{1}{r^{3/2}}[-\sin\tfrac{3}{2}\beta + \sin\tfrac{7}{2}\beta], \\ \overline{U}_{jj}^{\mathrm{I}} &= (1+\nu)C\frac{1}{r^{3/2}}\cos\tfrac{3}{2}\beta; \end{aligned} \tag{18}$$

Mode II:

$$\overline{U}_{11}^{\mathrm{I}} = -\frac{C}{8}\frac{1}{r^{3/2}}[5\sin\tfrac{3}{2}\beta + 3\sin\tfrac{7}{2}\beta], \qquad \overline{U}_{33}^{\mathrm{II}} = -\nu C\frac{1}{r^{3/2}}\sin(\tfrac{3}{2}\beta),$$

$$\overline{U}^{\mathrm{II}}_{22} = \overline{U}^{\mathrm{I}}_{12}, \quad \overline{U}^{\mathrm{II}}_{12} = \overline{U}^{\mathrm{I}}_{11},$$

$$\overline{U}^{\mathrm{II}}_{jj} = -(1-\nu)C\frac{1}{r^{3/2}}\sin\tfrac{3}{2}\beta;$$

Mode III:

$$\overline{U}^{\mathrm{III}}_{23} = \frac{(1-\nu)C}{2}\frac{1}{r^{3/2}}\cos\tfrac{3}{2}\beta, \qquad \overline{U}^{\mathrm{III}}_{13} = -\frac{(1-\nu)C}{2}\frac{1}{r^{3/2}}\sin\tfrac{3}{2}\beta. \tag{19}$$

In (18) to (19), $\overline{U}^{\alpha}_{ij} = \overline{U}^{\alpha}_{ji}$, and the rest of the components $\overline{U}^{\alpha}_{ij}$ are zero. The constant C is defined as

$$C = \frac{1}{2(1-\nu)\sqrt{2\pi}}. \tag{20}$$

Using (16) and (18) the influence of the transformation strains on the mode I stress intensity at the crack tip is given by

$$dk_{\mathrm{I}}^{\mathrm{TIP}} = G\frac{C}{4}\left\{\frac{1}{r^{3/2}}[\cos\tfrac{3}{2}\beta + 3\cos\tfrac{7}{2}\beta]e^{p}_{11} + \frac{1}{r^{3/2}}[7\cos\tfrac{3}{2}\beta - 3\cos\tfrac{7}{2}\beta]e^{p}_{22}\right.$$

$$\left. + \frac{6}{r^{3/2}}[-\sin\tfrac{3}{2}\beta + \sin\tfrac{7}{2}\beta]e^{p}_{12}\right\} \mathrm{d}A \tag{21}$$

which can be rewritten in complex variable notation as

$$dk_{\mathrm{I}}^{\mathrm{TIP}} = G\frac{C}{4}\,\mathrm{Re}\left\{\frac{1}{r^{3/2}}(e^{p}_{11} + 7e^{p}_{22} - 6ie^{p}_{12})[\cos\tfrac{3}{2}\beta - i\sin\tfrac{3}{2}\beta]\right.$$

$$\left. + \frac{3}{r^{3/2}}(e^{p}_{11} - e^{p}_{22} + 2ie^{p}_{12})[\cos\tfrac{7}{2}\beta - i\sin\tfrac{7}{2}\beta]\right\} \mathrm{d}A \tag{22}$$

($i^2 = -1$, and Re and Im denote the real and imaginary parts, respectively). Defining a complex variable $z = r\exp(i\beta)$, it follows that

$$\frac{1}{r^{3/2}}(\cos\tfrac{3}{2}\beta - i\sin\tfrac{3}{2}\beta) = \frac{1}{z^{3/2}} \quad \text{and} \quad \frac{1}{r^{3/2}}(\cos\tfrac{7}{2}\beta - i\sin\tfrac{7}{2}\beta) = \frac{\bar{z}}{z^{5/2}}, \tag{23}$$

where $\bar{z}$ denotes the complex conjugate of z, so that (22) can be rewritten as

$$dk_{\mathrm{I}}^{\mathrm{TIP}} = G\frac{C}{4}\,\mathrm{Re}\left\{\frac{1}{z^{3/2}}(e^{p}_{11} + 7e^{p}_{22} - 6ie^{p}_{12}) + \frac{3\bar{z}}{z^{5/2}}(e^{p}_{11} - e^{p}_{22} + 2ie^{p}_{12})\right\} \mathrm{d}A. \tag{24}$$

When the transformation strain distribution is symmetric with respect to $\xi_2 = 0$ this expression reduces to the integrand in the domain integral (27) given in [1].

For the influence on the mode II stress intensity at the crack tip the solution can be obtained along similar lines. It finally follows that

$$dk_{\mathrm{II}}^{\mathrm{TIP}} = G\frac{C}{4}\,\mathrm{Im}\left\{\frac{1}{z^{3/2}}(5e^{p}_{11} + 3e^{p}_{22} + 2ie^{p}_{12}) + \frac{3\bar{z}}{z^{5/2}}(e^{p}_{11} - e^{p}_{22} + 2ie^{p}_{12})\right\} \mathrm{d}A. \tag{25}$$

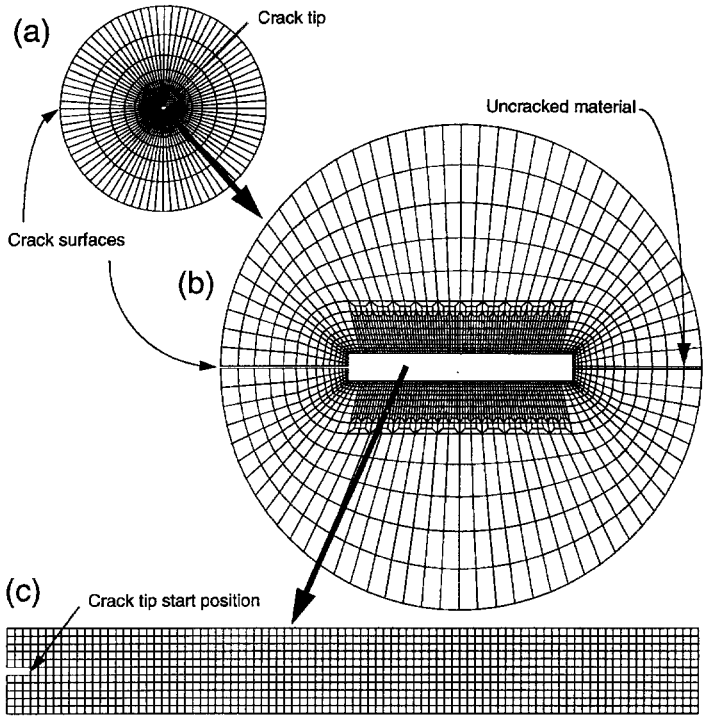

Figure 3. The finite element mesh used to analyse the small-scale crack growth problem. The mesh comprises 12096 quadrilateral elements and 12218 nodes. The crack is modelled by a missing row of elements.

The expressions (24) and (25) have to be integrated over the entire domain Ω to find the total influence of the transformation zone on the stress intensity factor at the tip,

$$\Delta k_\alpha^{\mathrm{TIP}} = \int\int_\Omega dk_\alpha^{\mathrm{TIP}}. \tag{26}$$

4. Numerical method

In [1], crack growth is simulated numerically with the aid of a nodal release technique. Here, in order to allow for crack deflection and meandering of the crack, we use an element vanish technique. The basic idea is similar to that used in, for instance, [11] and [12], but the actual crack criterion is different. We first discuss the finite element mesh and the implications of the element vanish approach, and then describe the implementation of the crack propagation criterion as described in Section 2.3.

4.1. The finite element mesh

A direct consequence of the introduction of a non-symmetric distribution of transformable phase is that the entire region Ω (see Figure 3 in [1]) defined for the small scale transformation problem has to be analyzed: Firstly, because of the loss of symmetry of the microstructure and secondly, because the inhomogeneity may cause a mode II loading component locally at the crack tip, which will cause the crack to deflect.

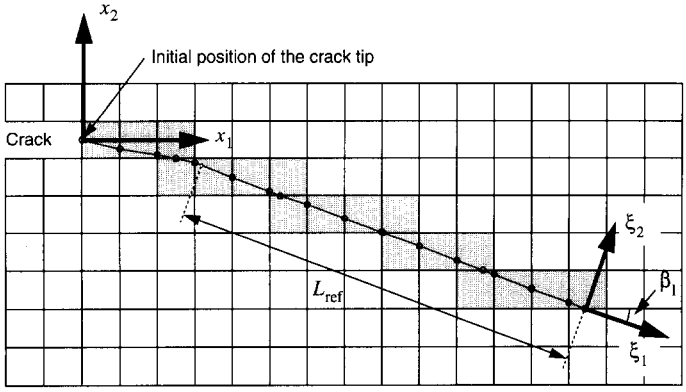

Figure 4. Crack growth using an element vanishing technique. The shaded elements represent the vanished elements, and the dots indicate the subsequent crack tip positions during crack propagation.

The mesh, shown in Figure 3, is therefore twice as large as that in Part I [1]. The lower half of the new mesh is obtained by reflection of the upper half, which is identical to the mesh in [1]. Where the material is not cracked, the two halves are connected with an extra row of elements. The crack is modelled by simply leaving out elements, as can be seen in Figure 3b and c. It can also be seen in Figure 3c that, initially, the crack tip is placed at three elements to the right of the left hand side of the rectangular region of the mesh.

Since the crack is now modelled by a missing row of elements, it has the same width as an element in the present discretization. The crack is no longer sharp but has a notch-like geometry (cf. [12]). In general, if the length of the crack is large compared to this width, the notch-like geometry asymptotically approaches to the geometry of a sharp crack. However, in our small scale approach the length of the crack is not defined, and the so-called characteristic length L (as defined in [1]) governs the scaling of the crack problem, and in particular it governs the size of the transformation zone. By increasing the value of L, the number of elements over the height of the transformation zone increases and the relative width of the crack decreases. Thus, for large values of the characteristic length L, the notch geometry approaches a sharp crack. This is a preferred situation if we want to compare the results with our previous analyses where the crack was indeed sharp [1]. Test computations with symmetric phase transformation distributions for increasing values of L showed convergence to results for a sharp crack. Also, additional computations were performed with a special mesh, where the height of the middle row of elements was reduced to simulate a sharp crack. These computations proved that in the limiting case our analysis is fully compatible with the computations for a sharp crack geometry in [1].

4.2. Discretization of the crack growth formulation

Figure 4 illustrates the procedure that is implemented in order to simulate crack growth. The initial position of the (actually sharp) crack tip is taken to be located half-way to the height of the leading element, as indicated in Figure 4. Starting from this initial configuration, if the critical stress intensity at the crack tip is reached according to (12), crack growth is simulated using an element vanishing technique. The stiffness and the stresses of that particular element are linearly reduced to zero in n steps. The number of steps n is usually 5 to 10, but for some

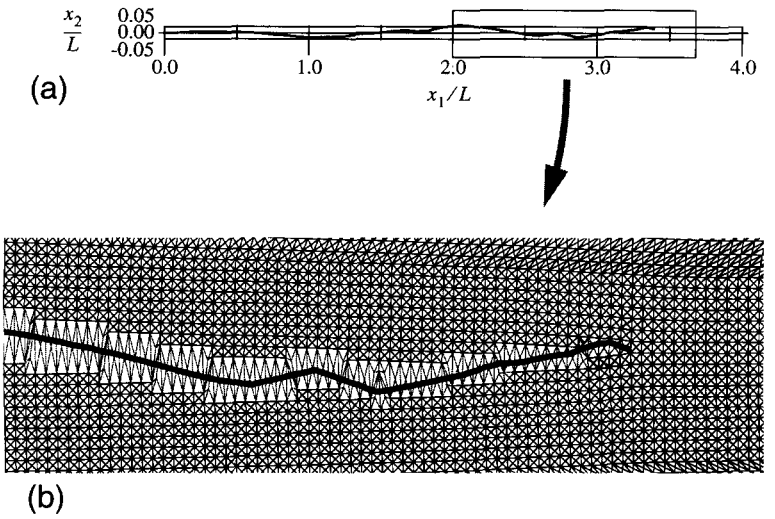

Figure 5. Crack path for $\omega = 15, \alpha = 1.15, h_0 = 0.0$ and $M = -\infty$. $\lambda_c = 2$ and $y_c = 0.25L_c$; (a) shows the unscaled deflection of the crack due to the inhomogeneity of the transformable phase, and in (b) part of the deformed crack geometry with the crack path is shown. The deformations are scaled by a factor 5.

computations with higher values of the transformation strength ω, n had to be much larger to keep the solution process stable.

Once the direction in which the crack wants to propagate β_m is determined on the basis of (14), the new position of the crack tip is found by drawing a straight line from the previous position under an angle β_m. Thus, the crack tip is now positioned at the intersection of that line with the edge of an adjacent element. When the element through which the crack just propagated has vanished, the stress intensity at the tip can be determined and the load can be increased again to reach the critical stress intensity. In this way, the crack can propagate through the mesh as shown by the enlarged crack tip area in Figure 4. The grey elements represent the elements which have vanished during the loading process. The crack path as obtained with the above procedure is also marked, and the positions of the crack tips during the discrete crack growth process are indicated by small circles.

During each step, the direction β_l of the crack has to be established. However, there is not one unique way to do so. We have chosen a method where a straight line with a certain length L_{ref} is fitted through the previous crack tip positions within the range L_{ref}, using the method of least squares. The smallest L_{ref} which can be taken would include only the current crack tip position and the previous one. It was found that the stability of the computations relied quite sensitively on the choice of L_{ref}, and that it was the smallest L_{ref} possible which gave the most stable solution. This value has been used in all computations.

On the circular outer boundary of Ω the displacements are prescribed again in correspondence with the far-field elastic solution, but in contrast to the previous analyses, the change in distance from the crack tip to each individual boundary node during crack growth is neglected. This is a reasonable approximation since in all computations, the distance from the crack tip to the boundary is much larger than the crack advance.

A typical result for the computed crack path in terms of crack displacements Δa_x and Δa_y is given in Figure 5. In Figure 5a the true scale crack path has been plotted , while Figure 5b gives a magnified view of a piece of the crack path, with all deformations of the crack tip

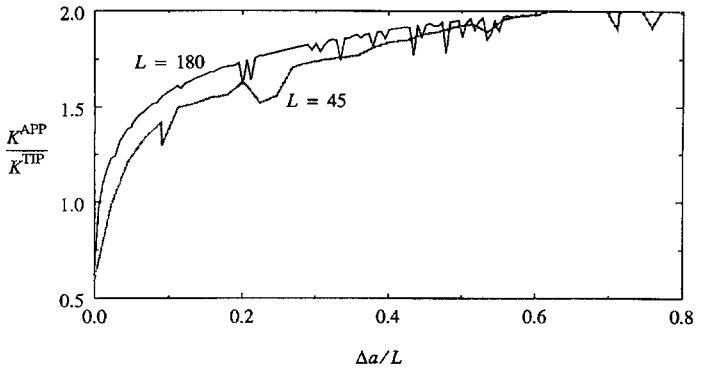

Figure 6. Two crack growth resistance curves for equal model parameters ($\omega = 15, \alpha = 1.15, h_0 = 1.25, \lambda_c = 2, y_c = 0.25L_c$) but computed with different accuracies, to check the convergence; (a) for $L = 45$, (b) for $L = 180$.

geometry being scaled by a factor 5. In the subsequent discussions, the deflection Δa_y away from the x_1-axis is usually scaled by a factor 10 to be able to see more detail. The elements drawn in grey represent the vanished elements which currently have zero stiffness. The results of this computation shall be discussed in more detail in Section 5.5. Each computation took about 12 CPU hours on a CRAY-YMP computer.

4.3. CONVERGENCE

Convergence of the computations has been checked by using more refined elements meshes. As demonstrated before [1], this can be done simply by increasing the scaling parameter L, defined in (31) of [1], while keeping all other model parameters constant. The predicted resistance curves in terms of the ratio K^{APP}/K^{TIP} have been plotted for $L = 45$ and 180, respectively, in Figure 6. The general shape of both curves are rather similar. Initially the curve of the more accurate computation ($L = 180$) rises more quickly, but after a crack growth of about $\Delta a/L = 0.5$, the results of the two computations are very similar. This behavior was also observed in the results for the symmetrical crack growth problem as reported in the companion paper [1]. In view of this, we can consider the results of the computation with $L = 45$ to be sufficiently converged.

Upon close examination, the irregularities in the computed resistance curves appear to be due to modelling errors in the domain integral. It turned out in particular that the change in local mode II stress intensity, Δk_{II}^{TIP}, according to (25)–(26) is very sensitive to the instantaneous position of the crack tip. This could cause a sudden tendency to drift away from the crack path, but in subsequent steps the crack was found to return to its expected crack path. From Figure 6 we can see that the 'dips' in the curves are equally deep. Apparently, these inaccuracies in the computation of the domain integral cannot be solved by increasing the fineness of the mesh. We tried to stabilize the process, for instance by means of some amount of under-relaxation, where the newly computed value for K^{TIP} was scaled a little towards the previous computed value of the stress intensity at the crack tip, but the results remained equally irregular.

In view of these observations, we decided to use the value of L equal to 45 in most of the results to be presented. Hence, in all these results, irregularities of the type seen in Figure 6 will be present, but we believe that these do not affect the general shape of the resistance curve. However, the results should only be interpreted in a qualitative way. In an attempt to

not let the 'dips' overshadow the general trend of the computations, we have included in all crack growth resistance curves presented, a smooth fit based on the polynomial representation

$$\frac{K^{\mathrm{APP}}}{K^{\mathrm{TIP}}}(\Delta a) = A_0 + A_1(\Delta a)^{A_2} + A_3(\Delta a)^{0.8} + A_4\cos(A_5\Delta a + A_6). \tag{27}$$

Here, $A_i (i = 1, \ldots, 6)$ are real-valued fit parameters.

5. Results

5.1. Starting position of the crack tip

First, some crack growth simulations have been performed over a distance of $2L$, with material parameters $\nu = 0.3, \alpha = 1.15, \omega = 5, h_0 = 1.25, M = -\infty, a = 1, \lambda_c = L_c/L = 2$ (see [1]). The distribution of transformable material as defined in (1)–(2) in [1] has been shifted relative to the initial crack tip position over various distances by choosing y_c in (1) according to

$$y_c \in [0, 0.125, 0.25, 0.375, 0.5]L_c \tag{28}$$

(recall that L_c is the period of the distribution function of the transformable phase, cf. (2) in [1]). As in [1], $C_A = 1$ for heterogeneous materials, so that the average density of transformable phase is the same as for the corresponding homogeneous material, $C_A = 0$. For $y_c = 0$ and $y_c = 0.5L_c$, the transformable phase is distributed symmetrically with respect to the x_1-axis, so that the crack does not deflect from its horizontal path $x_2 = 0$. Note that $y_c = 0$ corresponds to the cases studied in Part I [1]. For all other values of y_c, the distribution is not positioned symmetrically and the crack does deflect.

The results are shown in Figure 7. It is seen from Figure 7b that the deviation from the initial path is strongest for $y_c = 0.25L_c$ which corresponds to an anti-symmetric distribution of transformable phase relative to the x_1-axis. First the crack is attracted towards the area with less transformable phase, as crack growth in this area uses less energy. Then the crack starts to feel the influence of the large amount of transformable phase ahead, and at the same time the crack seems to be attracted towards the region with little transformable phase below. Thus, after a crack growth of about $L_c/6$ the sign of the angle between the x_1-axis and the tangent of the crack path changes from positive to negative. The crack crosses the x_1-axis and reaches a local minimum for $\Delta a \approx 2L_c/3$. The next region with a large amount of transformable material is approached and the crack smoothly deflects and grows towards the subsequent region of reduced transformable phase. Clearly, for the cases analyzed here, the crack meandering is directly linked to the distribution function of the transformable phase. The amplitudes of the deviations from the original crack path will probably depend on ω, as will be demonstrated later in Section 5.3. Quite remarkably, the paths for $y_c = 0.125L_c, 0.25L_c$ and $0.375L_c$ show a similar crack meandering behavior. Computations using y_c close to 0 or $0.5\lambda_c$ showed that the crack did not deflect and continued to grow along the x_1-axis.

The toughness development during crack growth is affected considerably by the value of y_c. In [1], where the crack was constrained to grow along a predetermined path by virtue of symmetry, it was found that the periodically varying amount of transformable phase caused oscillations in the crack growth resistance during crack growth. The results suggested that the maxima of the $K^{\mathrm{APP}}/K^{\mathrm{TIP}}$ vs. Δa curves always lie above the toughness curve for the

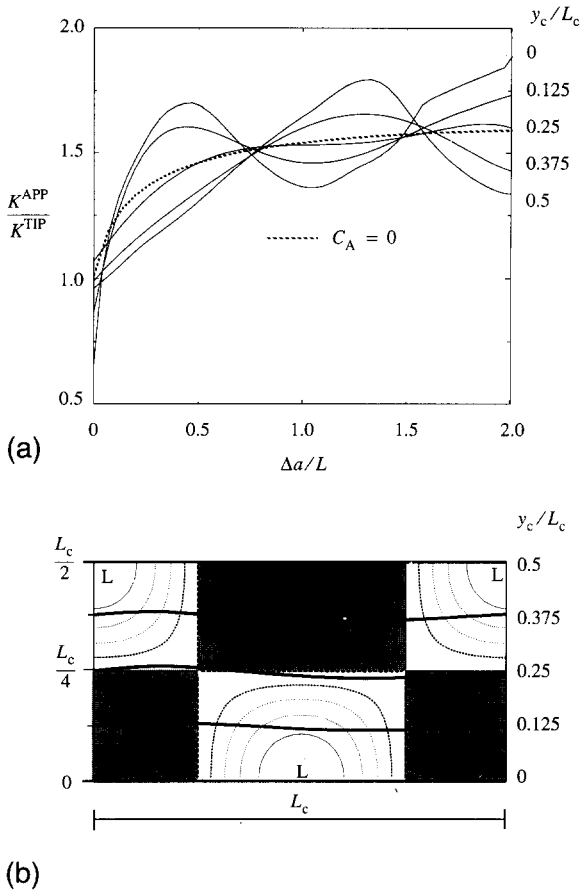

Figure 7. Crack growth resistance curves (a) and crack (b) for $\omega = 5, \alpha = 1.15, h_0 = 1.25, \lambda_c = 2$ and different initial positions of the crack tip $y_c = [0, 0.125, 0.25, 0.375, 0.5]L_c$. The results are compared with the crack growth resistance curve for a homogeneous material $C_A = 0$.

corresponding homogeneous material with the same average density of transformable phase. It was noted [1] that in the descending parts of the toughness curves, crack growth is unstable. The crack grows dynamically to the following region of high fraction of transformable material; in the simulation, however, dynamic crack growth effects have not been taken into account. One of such cases is recovered in Figure 7a for $y_c = 0$; the results are identical to those for $\lambda_c = 2$ in Figure 8 of [1]. We now see from Figure 7a that the oscillating behavior of the toughness is reduced for values of y_c closer to $0.25L_c$, while they increase again to similar values for y_c approaching $0.5L_c$ but with a 'phase shift'. Thus, the curves for the two symmetric cases, $y_c = 0$ and $y_c = 0.5L_c$, are the outer boundaries for the fluctuations. Still, all curves seem to oscillate around the solution for homogeneous materials ($C_A = 0$). It is noted in particular that for $y_c = 0.25L_c$, representing an anti-symmetric distribution of the transformable phase relative to the x_1-axis, the oscillations are very limited and the curve almost coincides with the crack growth resistance curve for the homogeneous material.

In contrast with the sensitivity of crack growth resistance to initial crack tip position, the actual meandering of the crack has been observed (Figure 7b) to be hardly influenced (except for the symmetric distributions). Here it should be realized that for the present set of

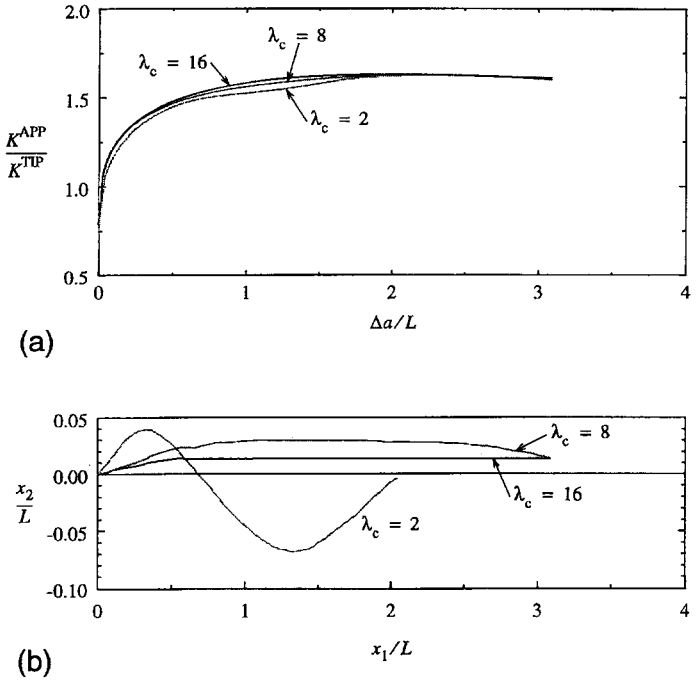

Figure 8. Crack growth resistance curves (a) and crack paths (b) for $\omega = 5, \alpha = 1.15, h_0 = 1.25, y_c = 0.25L_c$ and different lengths for the period of the heterogeneity in the distribution of transformable phase: $\lambda_c = 2, 8$ and 16.

material parameters, the 'height' of the transformation zone spans one or two periods L_c of the distribution, as can be seen in Figure 8b [1].

5.2. CHARACTERISTIC PERIOD OF THE INHOMOGENEITY

The influence of the characteristic period on the deflection behavior is studied by repeating the foregoing analyses with values of the period L_c corresponding to $\lambda_c = 8$ and 16. All other material parameters are kept unchanged: $\omega = 5, \alpha = 1.15, h_0 = 1.25$; and we focus on the case with $y_c = 0.25L_c$. As shown in Figure 8a, the computed crack growth resistance is only mildly dependent on L_c. The characteristic period of the transformable fraction for $\lambda_c = 16$ is so large compared to L that for $y_c = 0.25L_c$ the variations in the transformable fraction are not felt, and the crack resistance curve is similar to that for the homogeneous material ($C_A = 0$).

The crack paths for the three cases, shown in Figure 8b, show an interesting phenomenon. As expected, the period of the meandering crack matches the period of the heterogeneity of the transformable phase; but as the period of the heterogeneity λ_c increases, the meandering amplitude decreases. For $\lambda_c = 16$, the crack path seems to flatten out, and the crack propagates parallel to the x_1-axis. Apparently, the heterogeneities are too distant to be felt by the crack in this case, similar to the argument above concerning the crack resistance.

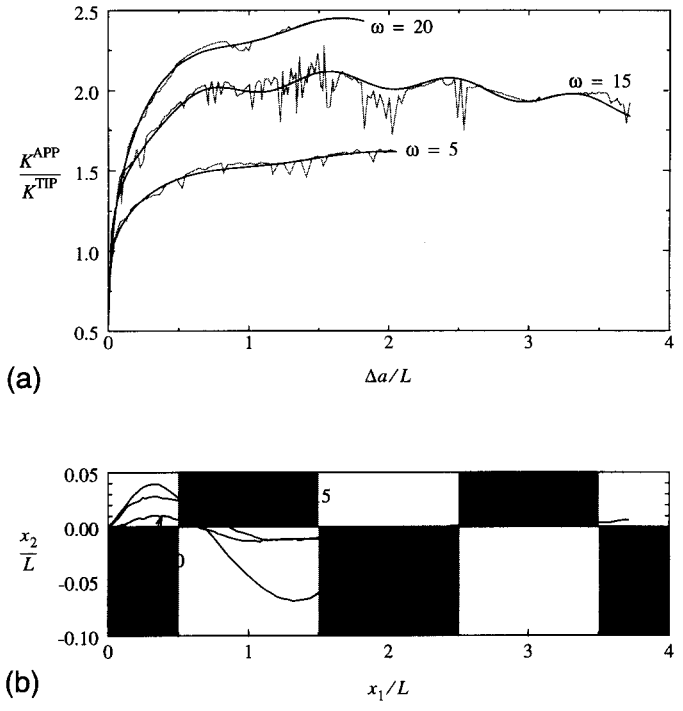

Figure 9. Crack growth resistance curves (a) and crack paths (b) for $\alpha = 1.15, h_0 = 1.25, \lambda_c = 2, y_c = 0.25L_c$ and various strengths of transformation: $\omega = 5, 15$ and 20. The shaded areas in (b) indicate the regions with a higher than average value of the density of transformable phase.

5.3. STRENGTH OF THE TRANSFORMATION

The influence of the strength of the transformation on the crack growth behavior is studied in Figure 9. For $\lambda_c = 2$ and $y_c = 0.25L_c$, and otherwise identical material parameters as before, Figure 8 gives results for $\omega = 5, 15$ and 20. As expected (cf. e.g. [1] [20]), also when the crack is free to meander, the toughness of the material increases when ω increases. Especially for $\omega = 15$ an oscillating behavior of the crack growth resistance curve is observed in Figure 9a.

As mentioned before, crack meandering around the x_1-axis occurs due to the fact that the region with the less than average transformable fraction seems to attract the crack, while a region with high transformable fraction seems to repulse the crack. It is interesting to notice that, as the transformation strength ω increases, the deviations from the original crack path diminish. For larger values of ω, the transformation strains seem to develop a relatively smaller shear stress intensity component. This stabilization behavior seems to become stronger as the crack propagates; for the larger values of ω and $\Delta a/L > 1$, the crack hardly deflects from its original path.

5.4. PURELY DILATANT TRANSFORMATION BEHAVIOR

In Figure 10 the results for a purely dilatant transforming material are presented. The material parameters used are the same as in Figure 9 for a strength specified by $\omega = 15$, but now with $h_0 = 0$ and $M = -10$. Also shown are some results for a material where transformation shear

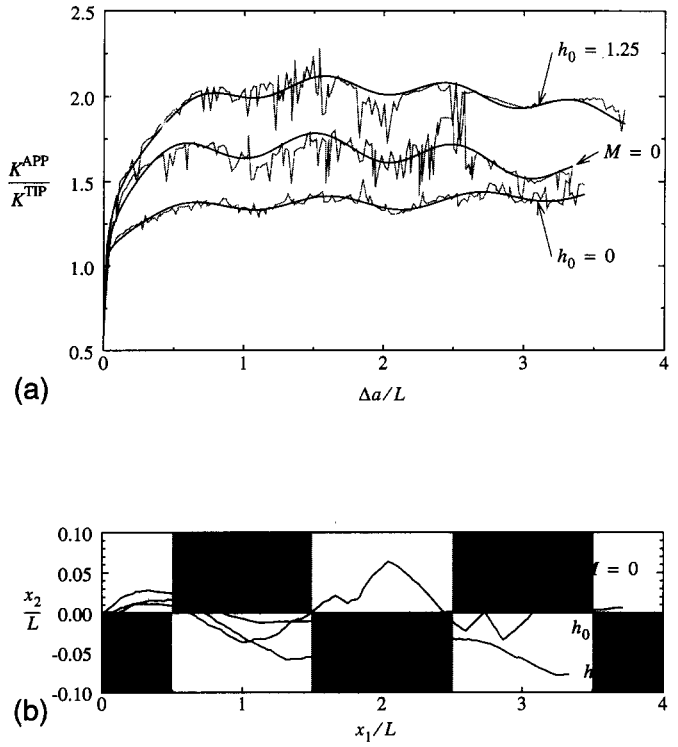

Figure 10. Crack growth resistance curves (a) and crack paths (b) for $\omega = 15, \alpha = 1.15, h_0 = 0$ (purely dilatant transformation) and $h_0 = 1.25$ (with dilatant and shear transformation), $\lambda_c = 2, y_c = 0.25L_c, M = -10$ (irreversible transformation) and $M - 0$ (with the possibility of reverse transformation). The shaded areas in (b) indicate the regions with a higher than average value of the density of the transformable phase.

strains do occur ($h_0 = 1.25$ as in Figure 9) but which exhibit reverse transformation, specified through $M = 0$. The latter case will be discussed in Section 5.5.

The crack growth resistance curve for the purely dilatant material shown in Figure 10a, shows clearly that the period of the oscillations is comparable to L_c. Note that the irregularities in the toughness curve (cf. Section 4.3) are smaller compared to those for the case with shear transformation strains, $h_0 = 1.25$. Apparently, the solution strategy described in Section 2 is more stable for dilatant transforming materials. On the other hand, it also gives at least, partial evidence for sensitivity of the procedure on the instantaneous value of $\Delta k_{\mathrm{II}}^{\mathrm{TIP}}$, which is to a large extent determined by the shear transformation strains.

The crack deflection behavior for these materials is also different than for the material that does exhibit shear transformation effects (see Figure 10b). The crack does oscillate during crack growth, but remains below the x_1-axis after it crosses the axis at $\Delta a/L = 0.7$. There appears to be a tendency for the crack to approach the symmetry axis of the distribution of the transformable phase at $x_2/L = -0.05$; but, further crack growth would be necessary to establish full confidence in this matter. The stabilizing effect of the transformation strain upon crack growth seems to be less then for materials which exhibit both dilatant and shear transformation strains.

5.5. REVERSE TRANSFORMATION

Upon crack growth, the material in the wake of the crack unloads. Reverse transformation of the transformation strains may take place in this area, as discussed for homogeneous materials in [20]. As it is suspected that the wake of the crack tends to reduce the deflection from the straight crack path, a computation with $M = 0$ is performed, so that complete reverse transformation is possible. All other material parameters were kept equal to those in the previous section with $h_0 = 1.25$. The results are shown again in Figure 10 (the crack path is also shown in Figure 5). Comparing the results for $M = 0$ with those without reverse transformation ($M = -10$), it is seen that there is much less 'damping' of the crack meandering. The crack keeps meandering with a more or less constant amplitude around the x_1-axis. Indeed, this is an indication that in non-reversible transforming materials the development of a large transformed wake has a stabilizing effect on the crack growth behavior. As expected (cf. [20]), the crack growth resistance is reduced when reverse transformation takes place in the wake of the crack (see Figure 10a).

5.6. DUPLEX CERAMICS

Similar to the cases which have been analyzed in Part I on the basis of the distribution (3) of [1], we here take $\omega = 15, \alpha = 1.15, h_0 = 1.25, \lambda_c = 0.56$, and consider three initial crack tip positions relative to the distribution of transformable phase: $y_c/L_c = 0$, 0.083 and 0.25, respectively. The results of these computations are given in Figure 11. The crack growth resistance curves are plotted in Figure 11a, while the crack paths for $y_c/L_c = 0.083$ and 0.25 are shown in Figure 11b. The crack paths have also been plotted in Figure 11c and d where the transformation zone is also given; in the latter plots the crack paths are plotted on a true scale.

According to Figure 11a, the toughness varies greatly during crack growth. As the crack approaches a transformable inclusion, the material in the inclusion starts to transform. Transformation in front of the crack tip ($\beta < 60°$) has an embrittling effect (see [1], [20]), and the toughness decreases. When the crack starts to grow into the inclusion the toughness increases strongly and reaches a maximum just before the crack leaves the inclusion. At that position, all transformed material is in the wake of the crack and thus helps to toughen the material. This toughness behavior is best demonstrated for the symmetric case $y_c = 0$, already discussed in [1].

When the crack tip is initially placed at $y_c = 0.25L_c$, the crack meanders between the transformable inclusions (see Figure 11c). This implies that there is virtually no toughening of the material, $K^{\text{APP}} \approx K^{\text{TIP}}$, even though there is a slight increasing when the crack tip is close to an inclusion (see Figure 11a). However, if the initial crack tip is placed at $y_c = 0.083L_c$, as shown in Figure 11d, the crack tip starts inside an inclusion and as the crack propagates the toughness increases, although not as high as for the case $y_c = 0$. Hence, we conclude that for the periodic distributions of inclusions considered here, we find the best possible toughening behavior for the symmetrical case, $y_c = 0$, and we find the worst possible toughening behavior for $y_c = 0.25L_c$.

The crack paths for $y_c = 0.083L_c$ and $y_c = 0.25L_c$ are very similar, as shown in Figure 11b. Note that the crack path for $y_c = 0.25L_c$ is relatively smooth. This indicates that the crack deflection process becomes less sensitive to model errors when the transformation strains are not located in the direct vicinity of the crack tip. Figure 11b and c indicate that, although

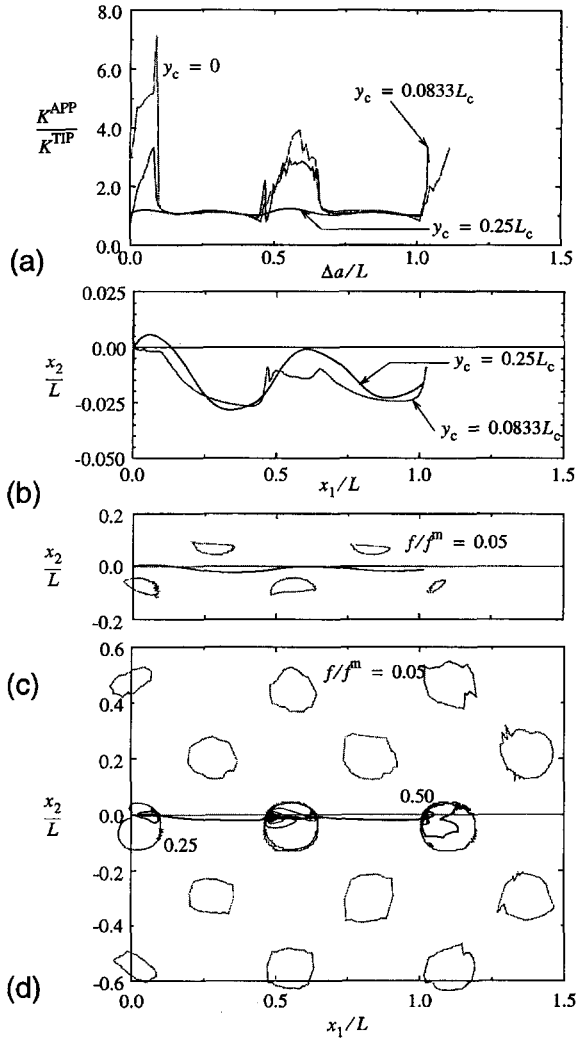

Figure 11. Crack growth resistance curves (a) and crack paths (b) for Duplex Ceramics with $\omega = 15, \alpha = 1.15, h_0 = 1.25, \lambda_c = 0.56$ and different initial positions of the crack tip: $y_c/L_c = 0.083$ and 0.25. Plots (c) and (d) show the crack path on true scale and the transformed inclusions, for $y_c/L_c = 0.083$ and 0.25, respectively.

the crack is repulsed by the inclusions, it tends to grow toward the axis of symmetry. This observation is even more clearly shown for $y_c = 0.083L_c$ in plot d. The crack propagates along a rather straight path through the inclusion, but once the tip is in the matrix it tends to grow toward the axis of symmetry. However, when the tip reaches a position somewhat before an inclusion, and material in the inclusion starts to transform, the crack tries to deflect around the inclusion. This is unsuccessful and the crack enters the inclusion. It proceeds again along a straight path until it re-enters the matrix, and again the crack grows toward the axis of symmetry.

Close examination of the transformation zone for $y_c = 0.25L_c$ showed that in this case the inclusions are only transformed for about 10 percent. Since the only contours plotted are $f/f^{\max} = 0.05, 0.25, 0.5$ and 0.75 (for $f^{\max} = 1$), the only contour plotted in Figure 11c is the one for $f/f^{\max} = 0.05$. For the case $y_c = 0.083L_c$ the transformation zone is plotted

in Figure 11d. For the inclusions where the crack passes through, the transformation is completed next to the crack surface. These inclusions are transformed for over 25 percent. For the inclusions further away from the crack surface, the 5 percent contour applies. More inclusions are transformed than for $y_c = 0.25L_c$ since the applied stress intensity K^{APP} had to be increased over $3K^C$ for the crack to grow when $\Delta a/L = 0.08$.

Lutz et al. [23] define two types of toughening behavior for their Duplex Ceramics, namely short-range and long-range toughening. For each category they observed typical crack paths. They found that for the short-range materials which are porous, microcracking occurs in the inclusion during crack growth. However, for decreasing porosity they find that the microcracking activity decreases and fully disappears for dense ceramic. In these dense materials very narrow transformation zones are found. Usually only the inclusions through which the crack has passed are found to be monoclinic. The crack path development for these types of material looks very much like the results we obtained in Figure 11d. Note however that in our analysis we did not account for any microcracking.

6. Discussion and conclusion

The most important conclusion from the analyses reported on in Part I [1] and in the present Part II is that a non-homogeneously distributed transformable phase causes the toughness to fluctuate during crack growth. From our analyses we find that at least some of the peaks of the fluctuations rise higher that the crack growth resistance curve for the homogeneous material with the same average density of transformed material.

We modelled ZTA materials by using smooth periodic distributions to investigate the influence of a non-homogeneously distributed transformable phase and we found oscillating toughness curves. The toughness increases when the crack grows through an area with a high density of transformable phase, reaching a maximum when it *approaches* an area with low transformable phase. This behavior is readily understood by recalling that the transformation strains behind the crack tip ($\beta > 60°$) tend to toughen the material, whereas transformation ahead of the tip $\beta < 60°$ tend to embrittle the material. For Duplex Ceramics, modelled with clusters of transformable phase, a similar behavior is found. However, the oscillations are less smooth and the peaks are usually higher. Since the highest value of $K^{\text{APP}}/K^{\text{TIP}}$ in our simulations is what determines the actual crack growth resistance, we may conclude that the heterogeneous materials may be tougher than the corresponding homogeneous materials.

However, the results in this part for non-symmetric distributions show that the crack can deflect towards a crack path which consumes less energy. The transformation strains can cause a mode II stress intensity component locally at the crack tip, causing the crack to deflect. It is found that regions in the material with a higher than average amount of transformable phase tend to repulse the crack, and that the crack tends to grow towards areas with a lower transformable fraction. However, the deflections found are rather small compared with the spatial variation of the transformable phase, so that the crack usually cannot avoid a dense area completely. The resulting crack meandering gives rise to oscillations in the crack growth resistance curve of a smaller amplitude, i.e. the peak values of the toughness are lower, but they remain higher than the maximum value for the homogeneous material.

It should be noted that the results for the non-symmetric distributions presented in this part should only be interpreted qualitatively, since the computation of the transformation domain integral in the deflected crack geometry is only valid for small deflections. The present computations only showed relatively small deflections, thereby validating the approach. However,

attempts to analyze far-field mixed mode loading failed, since the deflection angles were too large. It was also found that small changes in the angle for which the transformation domain integral were calculated resulted in large changes in the solution of the integral. For these reasons, we do not have full confidence in the quantitative results as even small errors in direction may build up during the crack growth process. Unfortunately, the magnitude of these errors cannot be quantified since direct methods are not available at this time: concepts such as the J-integral [21] and the stiffness derivative method [22] are only valid for straight cracks. However, we can conclude that the crack growth resistance curves found for homogeneous materials provide a lower bound to the simulations, while those for symmetric heterogeneous distributions [1] give an upper bound.

Our results for different lengths of the characteristic period of the distribution of transformable phase L_c showed a remarkably small influence on the toughness. The crack path however was shown to be directly related to L_c; the period of the crack path meandering around the x_1-axis of the crack path is almost the same as L_c for all cases analyzed.

Computations for various strengths of the transformation ω showed that for increasing strength the deflections of the crack from its original crack path decrease. For small crack extensions the crack still deflects, but for larger extensions the crack starts to proceed just about straight forward. The wake of the crack seems to stabilize the crack extension. This conclusion is confirmed by a computation for a material with reverse transformation in the wake of the crack, where we find a constant crack deflection behavior.

For Duplex Ceramics we found a crack path which was very similar to a crack behavior described by Lutz et al. [23] for what they termed a 'short-range toughened material'. The deflection of the crack path, relative to the inclusions size and spacing, is limited and only the inclusions close to the crack surface are transformed, while there is no micro-cracking. In our analyses we have not accounted for microcracking, and the transformation zone is very similar in shape. Peak toughness values are found to be very high for a crack which grows through the centers of the inclusions (symmetric distribution), but lower for crack paths which do not grow through the centers. Toughness is minimal for an initial position of the tip in the matrix and in between the inclusions ($y_c = 0.25L_c$). In this case, the crack does not grow through any inclusion, and the initial (matrix) toughness is hardly improved. This also shows the limitation of the use of a periodic distribution for the transformable inclusions. In reality, the inclusions will be distributed randomly and sooner or later the crack will grow into an inclusion, thereby improving the toughness of the composite. Another limitation of this analysis is that it is two-dimensional, where in practice the crack tip is a line and the distribution of the transformable phase will also vary in this third (x_3) direction.

Finally, it is appropriate to emphasize that this entire study has employed a continuum description of the material, both in terms of the heterogeneity studied here (for ZTA materials) and in terms of the constitutive response. Hence, there is an inherent limitation to the length scale of the phenomena that can be described with this type of modelling. In particular for ZTA materials it should be noted that the results of this study are only relevant when the actual transformation zone is wide enough to span a sufficiently large number of zirconia grains for the continuum modelling to be meaningful.

Acknowledgments

The work of Geert Stam was made possible by the Netherlands Organization for Scientific Research (NWO). The computing time on the Cray-YMP of the National Computing Facilities (NCF) Foundation in The Netherlands is gratefully acknowleged.

References

1. G.Th.M. Stam and E. van der Giessen, Crack growth in non-homogeneous transformable ceramics. Part I: Constrained straight cracks, *International Journal of Fracture* 79 (1996) 249–271.
2. S. Suresh, C.F. Shih, A. Morrone and N.P. O'Dowd, *Journal of the American Ceramics Society* 73 (1990) 1257–1267.
3. M-Y. He, A. Bartlett, A.G. Evans and J.W. Hutchinson, *Journal of the American Ceramics Society* 74 (1991) 767–771.
4. A.A. Rubinstein, *Journal of Applied Mechanics* 57 (1990) 97–103.
5. F. Erdogan, G.D. Gupta and M. Ratwani, *Journal of Applied Mechanics* 41 (1974) 1007–1013.
6. K. Hayashi and S. Nemat-Nasser, *Journal of Applied Mechanics* 48 (1981) 520–524.
7. B.L. Karihaloo, L.M. Keer, S. Nemat-Nasser and A. Oranatnachai, *Journal of Applied Mechanics* 48 (1981) 515–519.
8. B. Cotterel and J.R. Rice, *International Journal of Fracture* 16 (1980) 155–170.
9. A.R. Ingraffea and V. Saouma, in *Fracture Mechanics of Concrete*, G.C Sih and A. DiTommaso (eds.) Martinus Nijhoff, Dordrecht (1985) 171–222.
10. J. Wang, P. Navi and C. Huet, in *Proceedings FraMCoSI*, Z.P. Bazant (ed.), Elsevier, London/New York (1992) 373–378.
11. V. Tvergaard, *Journal of Mechanics and Physics of Solids* 30 (1982) 399–425.
12. M. Ortiz and A.E. Giannakopoulos, *International Journal of Fracture* 44 (1990) 233–258.
13. X.P. Xu and A. Needleman, *Journal of Mechanics and Physics of Solids* 42 (1994) 1397–1434.
14. D. Broek, *Elementary Engineering Fracture Mechanics*, Martinus Nijhoff Publishers, The Hague, The Netherlands (1982).
15. S. Suresh and C.F. Shih, *International Journal of Fracture* 30 (1986) 237–259.
16. J.W. Hutchinson, Harvard University Report TR74-1042 (1974).
17. H. Gao, *Journal of Mechanics and Physics of Solids* 37 (1989) 133–153.
18. J.R. Rice, *International Journal of Solids and Structures* 21 (1985) 781–791.
19. H.F. Bueckner, *International Journal of Solids and Structures* 23 (1987) 57–93.
20. G.Th.M. Stam and E. Van der Giessen, *Mechanics of Materials* 21 (1995) 51–71.
21. J.R. Rice, in *Fracture*, Volume 2, H. Liebowitz (ed.) (1968) 191–311.
22. D.M. Parks, *International Journal of Fracture* 10 (1974) 487–501.
23. E.H. Lutz, N. Claussen and M.V. Swain, *Journal of the American Ceramics Society* 74 (1991) 11–18.